Chaos, Solitons and Fractals 191 (2025) 115870

Contents lists available at ScienceDirect

Chaos, Solitons and Fractals

journal homepage: www.elsevier.com/locate/chaos

Variable Kerr nonlinearity and optical bistability of a four-level lambda atomic medium

Luong Thi Yen Nga [a], Nguyen Huy Bang [a], Nguyen Van Phu [a], Hoang Minh Dong [b], Nguyen Thi Thu Hien [b], Nguyen Van Ai [c], Le Van Doai [a,*]

[a] Vinh University, 182 Le Duan Street, Vinh City, Viet Nam
[b] Ho Chi Minh City University of Industry and Trade, Ho Chi Minh City, Viet Nam
[c] Ha Tinh University, 26/3 Street, Ha Tinh City, Viet Nam

ARTICLE INFO

Keywords:
Kerr nonlinearity
Optical bistability
Electromagnetically induced transparency

ABSTRACT

Using perturbation theory we obtain expressions for the third-order nonlinear susceptibility and the Kerr nonlinear coefficient of a four-level lambda-type atomic system in the presence of Doppler broadening. The model is applied to the Rb atomic gas medium at room temperature; the investigations demonstrate the ability to enhance and control the Kerr nonlinear coefficient according to laser parameters in single-window and double-window EIT regimes. The amplitude and the sign of the Kerr nonlinear coefficient change sensitively to the driving laser parameters as well as ambient temperature. As a representative application, this Kerr nonlinear medium is applied to optical bistability (OB) and shows that the threshold intensity and the width of OB are also easily changed according to the laser parameters. In particular, in double-window EIT regime the emergence of nonlinear coefficient at different frequency domains that leads to the appearance of OB at multiple frequency domains simultaneously. This study is a good preparation for experimental observations of Kerr nonlinearity and optical bistability.

1. Introduction

The Kerr nonlinearity plays an important role in photonic devices such as optical bistability, all-optical switching, optical frequency conversion, optical logic gates, optical solitons, nonlinear wave mixing, etc., [1]. Large Kerr nonlinear coefficient is desired by researchers to reduce the threshold intensity and increase the sensitivity of nonlinear optical phenomena. Currently, a simple solution to achieve controllable giant Kerr nonlinearity is based on electromagnetically induced transparency (EIT) [2–4]. Thanks to this, nonlinear optical phenomena with single photon in EIT media have been realized [4–6].

Nowadays, the EIT effect is easily observed in alkali metal atoms at room temperature or ultracold in a magneto-optical trap (MOT) [7]. Initially, the EIT effect was observed in three-level atomic systems including lambda-type [8,9], ladder-type [10], and V-type [11] configurations with a single transparency window (EIT window). Later, studies were extended to multi-level atomic configurations with multiple EIT windows. For example, double EIT models in four-level atomic systems including N-type [12], inverted Y-type [13], Y-type [14], tripod-type [15] schemes as well as multi-EIT configurations of five-level system [16–19]. Experimentally, multi-window EIT has also been observed in the four-level [20–22] and five-level [23–25] atomic configurations. Among all the models of EIT [26], the lambda configuration is of more interest because it is easy to achieve high transparency efficiency and consequentially easy to observe experimentally.

Giant Kerr nonlinear coefficient of EIT media has also been observed in three-level atomic systems [27] with a pair of enhanced Kerr nonlinear peaks around the EIT window. It is also shown that the amplitude and the sign of the Kerr nonlinearity are controlled by the intensity and the frequency of the coupling laser beam. Similar to EIT, recent studies on Kerr nonlinearity are also directed towards multi-level atomic configurations that can generate multiple nonlinear peaks at EIT windows and its applications can be realized at different frequency regions simultaneously. For example, four-level [28–32] and five-level [33–35] configurations for the study of Kerr nonlinearity have been proposed. Besides atomic gas media, EIT-based nonlinear enhancement has also been realized in some solid media of quantum wells or semiconductors [36–41]. Additionally, along this same topic some recent

* Corresponding author.
E-mail address: doailv@vinhuni.edu.vn (L. Van Doai).

https://doi.org/10.1016/j.chaos.2024.115870
Received 28 October 2024; Received in revised form 18 November 2024; Accepted 29 November 2024
Available online 3 December 2024

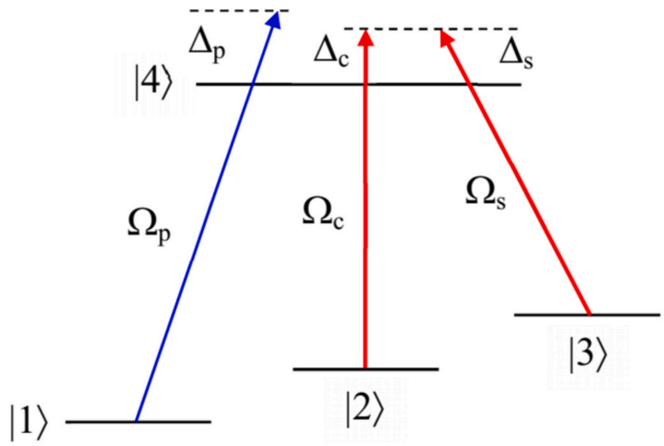

Fig. 1. The four-level lambda-type atomic configuration excited by a probe laser field and two driving laser fields.

studies have performed calculations up to the fifth order nonlinear susceptibility [42,43]. Experimentally, in addition to the above-mentioned three-level atomic configurations performed, experimental observations of Kerr nonlinearity have also been done in four-level N-type configurations [44,45], etc.

Optical bistability (OB) is perhaps one of the most typical applications of Kerr nonlinear material and is an important element in modern photonic devices. The OB effect with EIT medium was also proposed early in three-level atomic configurations [46–50]. In particular, the experimental observation of optical bistability by Min Xiao et al. [47] was made soon after the observation of the Kerr nonlinear coefficient of the three-level lambda-type atomic medium of Rb atom. Along with the interest of Kerr nonlinearity in four-level and five-level atomic systems, optical bistability has also been studied in the four-level [51–56] and five-level [57,58] atomic systems. In such multi-level configurations, OB can be simultaneously present at different frequencies. In addition, to change the threshold intensity and the width of OB, some studies have proposed to add other factors such as external magnetic field [59], polarization and relative phase between laser fields [60], incoherent pump field [61], etc. Similar to the nonlinear effect, EIT-based OB has also been of interest in solid-state materials of quantum wells and semiconductors [62–67].

In this work, we study the enhancement and the control of the Kerr nonlinear coefficient in a four-level lambda-type atomic medium. The atomic configuration is excited by a probe laser field and two driving laser fields with equal roles which can provide single-window and double-window EIT on the probe absorption profile. Analytical expressions for the Kerr nonlinear coefficient are derived in the absence and presence of the Doppler effect. Investigations of the Kerr nonlinear coefficient of Rb atoms with laser parameters are carried out in detail. In particular, as an application example, we have applied this Kerr nonlinear material to the study of optical bistability. The changes in amplitude and sign of the Kerr nonlinear coefficient are used to explain the changes in the threshold intensity and the width of OB. Experimentally, the lambda-type excitation configuration is known to have the best transparency performance among the possible excitation configurations and it is also easy to realize with Rb atoms, so this study is a good preparation for the experimental observation of Kerr nonlinearity and optical bistability.

2. Theoretical model and basic equations

The semi-classical theory which means the laser fields are illustrated according to classical theory while the atoms are illustrated in accordance with quantum mechanics is used to describe the interaction between the laser fields and the atoms. In this model, three laser fields with different frequencies are applied to the atomic system as follows: one weak probe laser field is specified with frequency ω_p and Rabi frequency Ω_p to excite the transition $|1\rangle \leftrightarrow |4\rangle$, while two strong driving laser fields are respectively named as the coupling laser field with frequency ω_c and Rabi frequency Ω_c to excite the transition $|2\rangle \leftrightarrow |4\rangle$ and the signal laser field with frequency ω_s and Rabi frequency Ω_s to excite the transition $|3\rangle \leftrightarrow |4\rangle$. Energy levels of this four-level atom are described in Fig. 1. Let Δ_p, Δ_c, and Δ_s be frequency detunings of probe field, coupling field, and signal field compared with the transition frequency from levels $|1\rangle$, $|2\rangle$ and $|3\rangle$ to level $|4\rangle$ with their formulas $\Delta_p = \omega_{41}$ - ω_p, $\Delta_c = \omega_{42}$ - ω_c and $\Delta_s = \omega_{43}$ - ω_s.

The density matrix method is also used to determine the atomic states through density matrix element ρ with $\rho = |\psi\rangle\langle\psi|$ and Schrodinger equation $i\hbar|\dot{\psi}\rangle = H|\psi\rangle$ is now substituted by Liouville equation:

$$\frac{\partial \rho}{\partial t} = -\frac{i}{\hbar}[H,\rho] - (\gamma\rho) \tag{1}$$

here, $(\gamma\rho)$ describes the relaxation processes in the atomic system.

Assuming that the strong driving laser fields only cause precise transitions of designated states and have no effect on any further levels. The total Hamiltonian of the system includes the Hamiltonian of the free atom and the interaction Hamiltonian of the light fields:

$$H_0 = \sum_{n=1}^{4} \hbar\omega_n |n\rangle\langle n| + \frac{\hbar\Omega_p}{2}|1\rangle\langle 4|e^{-i\omega_p t} + \frac{\hbar\Omega_c}{2}|2\rangle\langle 4|e^{-i\omega_c t} + \frac{\hbar\Omega_s}{2}|3\rangle\langle 4|e^{-i\omega_s t} + c.c \tag{2}$$

From Eqs. (2)–(6) and using the rotating wave approximation, the density matrix equations of the four-level system are written as:

$$\dot{\rho}_{11} = \Gamma_{41}\rho_{44} + \left(\frac{i\Omega_p}{2}\right)(\rho_{14} - \rho_{41}) \tag{3}$$

$$\dot{\rho}_{22} = \Gamma_{42}\rho_{44} + \left(\frac{i\Omega_c}{2}\right)(\rho_{24} - \rho_{42}) \tag{4}$$

$$\dot{\rho}_{33} = \Gamma_{43}\rho_{44} + \left(\frac{i\Omega_s}{2}\right)(\rho_{34} - \rho_{43}) \tag{5}$$

$$\dot{\rho}_{44} = -(\Gamma_{41} + \Gamma_{42} + \Gamma_{43})\rho_{44} + \left(\frac{i\Omega_p}{2}\right)(\rho_{41} - \rho_{14}) + \left(\frac{i\Omega_c}{2}\right)(\rho_{42} - \rho_{24}) + \left(\frac{i\Omega_s}{2}\right)(\rho_{43} - \rho_{34}) \tag{6}$$

$$\dot{\rho}_{21} = \left[i(\Delta_p - \Delta_c) - \gamma_{21}\right]\rho_{21} - \left(\frac{i\Omega_c}{2}\right)\rho_{41} + \left(\frac{i\Omega_p}{2}\right)\rho_{24} \tag{7}$$

$$\dot{\rho}_{31} = \left[i(\Delta_p - \Delta_s) - \gamma_{31}\right]\rho_{31} - \left(\frac{i\Omega_s}{2}\right)\rho_{41} + \left(\frac{i\Omega_p}{2}\right)\rho_{34} \tag{8}$$

$$\dot{\rho}_{32} = [i(\Delta_c - \Delta_s) - \gamma_{32}]\rho_{32} - \left(\frac{i\Omega_s}{2}\right)\rho_{42} + \left(\frac{i\Omega_c}{2}\right)\rho_{34} \tag{9}$$

$$\dot{\rho}_{41} = [i\Delta_p - \gamma_{41}]\rho_{41} - \left(\frac{i\Omega_p}{2}\right)(\rho_{11} - \rho_{44}) - \left(\frac{i\Omega_c}{2}\right)\rho_{21} - \left(\frac{i\Omega_s}{2}\right)\rho_{31} \tag{10}$$

$$\dot{\rho}_{42} = [i\Delta_c - \gamma_{42}]\rho_{42} - \left(\frac{i\Omega_c}{2}\right)(\rho_{22} - \rho_{44}) - \left(\frac{i\Omega_p}{2}\right)\rho_{12} - \left(\frac{i\Omega_s}{2}\right)\rho_{32} \tag{11}$$

$$\dot{\rho}_{43} = [i\Delta_s - \gamma_{43}]\rho_{43} - \left(\frac{i\Omega_s}{2}\right)(\rho_{33} - \rho_{44}) - \left(\frac{i\Omega_p}{2}\right)\rho_{13} - \left(\frac{i\Omega_c}{2}\right)\rho_{23} \tag{12}$$

The matrix elements describing population are interrelated through normalized condition:

$$\rho_{11} + \rho_{22} + \rho_{33} + \rho_{44} = 1 \tag{13}$$

where Γ_{mn} is the rate of spontaneous population decay from the level $|m\rangle$ to the level $|n\rangle$, and γ_{mn} is defined as the rate of the atomic coherence decay between the level $|m\rangle$ and the level $|n\rangle$.

To obtain the steady-state solutions for the density matrix element ρ_{41} in the higher-order perturbations, we need use a iterative technique, that the density matrix elements are expressed as [27] $\rho_{nm} = \rho_{nm}^{(0)} + \rho_{nm}^{(1)} + \rho_{nm}^{(2)} + \ldots$, where each successive approximation is calculated using the matrix elements of one order less than the one being calculated. Under the condition that the driving fields are much stronger than the probe field, then the density matrix eqs. (7), (8) and (10) in first-order perturbation can be written as:

$$0 = \left[i(\Delta_p - \Delta_c) - \gamma_{21}\right]\rho_{21}^{(1)} - \left(\frac{i\Omega_c}{2}\right)\rho_{41}^{(1)} + \left(\frac{i\Omega_p}{2}\right)\rho_{24}^{(0)} \tag{14}$$

$$0 = \left[i(\Delta_p - \Delta_s) - \gamma_{31}\right]\rho_{31}^{(1)} - \left(\frac{i\Omega_s}{2}\right)\rho_{41}^{(1)} + \left(\frac{i\Omega_p}{2}\right)\rho_{34}^{(0)} \tag{15}$$

$$0 = \left[i\Delta_p - \gamma_{41}\right]\rho_{41}^{(1)} - \left(\frac{i\Omega_p}{2}\right)\left(\rho_{11}^{(0)} - \rho_{44}^{(0)}\right) - \left(\frac{i\Omega_c}{2}\right)\rho_{21}^{(1)} - \left(\frac{i\Omega_s}{2}\right)\rho_{31}^{(1)} \tag{16}$$

In the weak probe field approximation, the terms $\left(\frac{i\Omega_p}{2}\right)\rho_{24}^{(0)}$ and $\left(\frac{i\Omega_p}{2}\right)\rho_{34}^{(0)}$ can be neglected, so the solution of the density matrix element ρ_{41} in first-order perturbation has the following form:

$$\rho_{41}^{(1)} = \frac{i\Omega_p\left(\rho_{44}^{(0)} - \rho_{11}^{(0)}\right)}{2F} \tag{17}$$

where, $F = \gamma_{41} - i\Delta_p + \frac{\Omega_c^2}{4\left[\gamma_{21} - i(\Delta_p - \Delta_c)\right]} + \frac{\Omega_s^2}{4\left[\gamma_{31} - i(\Delta_p - \Delta_s)\right]}$.

In a similar way, the solution of the density matrix element ρ_{41} in third-order perturbation as:

$$\rho_{41}^{(3)} = \frac{i\Omega_p\left(\rho_{44}^{(2)} - \rho_{11}^{(2)}\right)}{2F} \tag{18}$$

Thus, we need to determine $\rho_{44}^{(2)} - \rho_{11}^{(2)}$ in the second-order perturbation. We note that, by conservation of population of the four-level atomic system $\rho_{11}^{(0)} + \rho_{22}^{(0)} + \rho_{33}^{(0)} + \rho_{44}^{(0)} = 1$, while $\rho_{11}^{(k>0)} + \rho_{22}^{(k>0)} + \rho_{33}^{(k>0)} + \rho_{44}^{(k>0)} = 0$. In addition, due to the symmetry of the atomic gas medium, so that $\rho_{mn}^{(2)} = 0\ (m \neq n)$ [1]. In this configuration, we assume $\rho_{22}^{(2)} \approx \rho_{33}^{(2)} \approx 0$ because atoms are mainly in the ground state $|1\rangle$ and the excited state $|4\rangle$, so from eq. (13) we obtain:

$$\rho_{11}^{(2)} \approx -\rho_{44}^{(2)} \tag{19}$$

Then, eqs. (3) and (6) in the second-order perturbation have the forms:

$$0 = \Gamma_{41}\rho_{44}^{(2)} + \left(\frac{i\Omega_p}{2}\right)\left(\rho_{14}^{(1)} - \rho_{41}^{(1)}\right) \tag{20}$$

$$0 = -(\Gamma_{41} + \Gamma_{42} + \Gamma_{43})\rho_{44}^{(2)} + \left(\frac{i\Omega_p}{2}\right)\left(\rho_{41}^{(1)} - \rho_{14}^{(1)}\right) \tag{21}$$

Here, we neglected the terms $\rho_{42}^{(2)}$, $\rho_{24}^{(2)}$, $\rho_{43}^{(2)}$ and $\rho_{34}^{(2)}$ due to the symmetry of the atomic gas medium, and assume that the atoms initially are in the ground state $|1\rangle$, i.e. $\rho_{11}^{(0)} \approx 1$, $\rho_{22}^{(0)} \approx 0$ and $\rho_{33}^{(0)} \approx 0$.

From eqs. (19)–(21), we find:

$$\rho_{44}^{(2)} - \rho_{11}^{(2)} = \frac{2i\Omega_p}{2\Gamma_{41} + \Gamma_{42} + \Gamma_{43}}\left(\rho_{41}^{(1)} - \rho_{14}^{(1)}\right) \tag{22}$$

By substituting eq. (22) into eq. (18) and combining with eq. (17), we obtain the solution for ρ_{41} in third-order perturbation:

$$\rho_{21}^{(3)} = \frac{i\Omega_p}{F}\left(\frac{\Omega_p^2}{2\Gamma_{41} + \Gamma_{42} + \Gamma_{43}}\left[\frac{1}{F} + \frac{1}{F^*}\right]\right) \tag{23}$$

Finally, the solution for ρ_{41} up to the third-order perturbation has the form:

$$\rho_{41} = \rho_{41}^{(1)} + \rho_{41}^{(3)} = \frac{-i\Omega_p}{2F} + \frac{i\Omega_p}{F}\frac{\Omega_p^2}{2\Gamma_{41} + \Gamma_{42} + \Gamma_{43}}\left(\frac{1}{F} + \frac{1}{F^*}\right) \tag{24}$$

where, F^* is the complex conjugate of F.

The complex susceptibility (χ) of the atomic medium to the probe laser beam is related to the density matrix element ρ_{41} as follows:

$$\chi = -2\frac{Nd_{41}}{\varepsilon_0 E_p}\rho_{41} \equiv \frac{2Nd_{41}}{\varepsilon_0 E_p}\left[\frac{i\Omega_p}{2F} - \frac{i\Omega_p}{F}\frac{\Omega_p^2}{2\Gamma_{41} + \Gamma_{42} + \Gamma_{43}}\left(\frac{1}{F} + \frac{1}{F^*}\right)\right] \tag{25}$$

where N is the atomic density and ε_0 is the permittivity in vacuum.

On the other hand, we can write the expression for the susceptibility in terms of the perturbation orders as follows [1]:

$$\chi = \chi^{(1)} + 3E_p^2\chi^{(3)} \tag{26}$$

By comparing (25) and (26) we obtain the expressions for the first and third order susceptibilities as:

$$\chi^{(1)} = \frac{iNd_{41}^2}{\varepsilon_0\hbar}\frac{1}{F} \tag{27}$$

$$\chi^{(3)} = -\frac{iNd_{41}^4}{3\varepsilon_0\hbar^3}\frac{2}{2\Gamma_{41} + \Gamma_{42} + \Gamma_{43}}\frac{1}{F}\left(\frac{1}{F} + \frac{1}{F^*}\right) \tag{28}$$

For atomic vapor at room temperature, we need to introduce the Doppler effect in the expressions of the susceptibility. To eliminate the first-order Doppler effect, we assume that the driving and the probe laser beams propagate in the same direction through the atomic sample. Thus, if the atoms move with velocity v in the direction of the propagation of the laser beams, the frequency of laser beams is shifted by an amount $\omega_p + (v/c)\omega_p$, $\omega_c + (v/c)\omega_c$ and $\omega_s + (v/c)\omega_s$, respectively. This causes the frequency detuning of laser beams to increase by an amount $\Delta'_p = \Delta_p + (v/c)\omega_p$ và $\Delta'_c = \Delta_c + (v/c)\omega_c$ and $\Delta'_s = \Delta_s + (v/c)\omega_s$, respectively. The components of the atomic velocities along the beam axis follow the Maxwell distribution:

$$dN(v) = \frac{N_0}{u\sqrt{\pi}}e^{-v^2/u^2}dv, \tag{29}$$

where, $u = \sqrt{\frac{2k_BT}{m}}$ is the root-mean-square speed of the atoms, N_0 is the total atomic density in the sample. Thus, the first- and third-order susceptibilities when the Doppler effect is considered as:

$$\chi^{(1)}(v)dv = \frac{id_{41}^2}{\varepsilon_0\hbar}\frac{1}{F(v)}dN(v) \tag{30}$$

$$\chi^{(3)}(v)dv = -\frac{id_{41}^4}{3\varepsilon_0\hbar^3}\frac{1}{2\Gamma_{41} + \Gamma_{42} + \Gamma_{43}}\frac{1}{F(v)}\left[\frac{1}{F(v)} + \frac{1}{F^*(v)}\right]dN(v) \tag{31}$$

where,

$$\begin{aligned} F(v) = \gamma_{41} - i\left(\Delta_p + \frac{v}{c}\omega_p\right) &+ \frac{\Omega_c^2}{4\left[\gamma_{21} - i(\Delta_p - \Delta_c) - i\frac{v}{c}(\omega_p - \omega_c)\right]} \\ &+ \frac{\Omega_s^2}{4\left[\gamma_{31} - i(\Delta_p - \Delta_s) - i\frac{v}{c}(\omega_p - \omega_s)\right]} \end{aligned} \tag{32}$$

Performing the integration with v over $-\infty \to +\infty$, we get:

$$\chi^{(1)} = \frac{iN_0 d_{41}^2\sqrt{\pi}}{\varepsilon_0\hbar(\omega_p u/c)}\frac{1}{2\Gamma_{41} + \Gamma_{42} + \Gamma_{43}}e^{z^2}\left[1 - erf(z)\right] \tag{33}$$

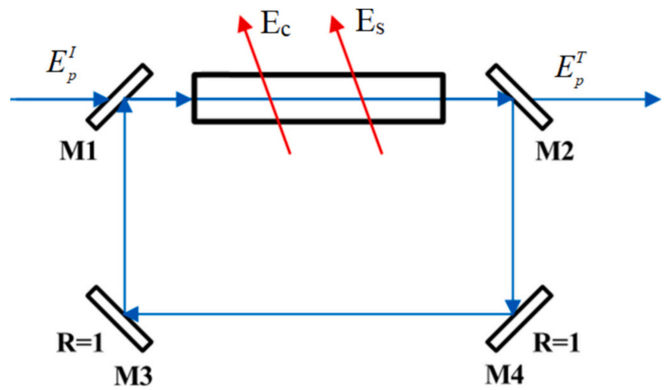

Fig. 2. Unidirectional ring cavity with atomic sample of length L, where, mirrors M1 and M2 have the refection and transmission coefficients as R and T with $R + T = 1$, whereas mirrors M3 and M4 are perfect reflectors. E_p^I and E_p^T denote the incident and transmitted probe field, respectively. E_c and $E_s$represent the coupling and signal fields that are not circulated inside the cavity.

$$\chi^{(3)} = -\frac{iN_0 d_{41}^4}{3\sqrt{\pi}\varepsilon_0\hbar^3(\omega_p u/c)^2}\frac{2}{2\Gamma_{41}+\Gamma_{42}+\Gamma_{43}}$$
$$\times\left\{2\sqrt{\pi}\left(-1+\sqrt{\pi}ze^{z^2}[1-erf(z)]\right)+\frac{\pi\left(e^{z^2}[1-erf(z)]+e^{z^{*2}}[1-erf(z^*)]\right)}{z+z^*}\right\} \tag{34}$$

where,

$$z = \frac{c}{\omega_p u}\left(\gamma_{41} - i\Delta_p + \frac{\Omega_c^2}{4[\gamma_{21} - i(\Delta_p - \Delta_c)]} + \frac{\Omega_s^2}{4[\gamma_{31} - i(\Delta_p - \Delta_s)]}\right) \tag{35}$$

and z^* is the complex conjugate of z, with erf being the error function.

The effective refractive index of the Kerr nonlinear medium for the probe laser beam as [1]:

$$n = n_0 + n_2 I_p \tag{36}$$

where:

$$n_0 = \sqrt{1 + Re(\chi^{(1)})} \tag{37}$$

is the linear dispersion coefficient, and:

$$n_2 = \frac{3Re(\chi^{(3)})}{4\varepsilon_0 n_0^2 c} \tag{38}$$

is the Kerr nonlinear coefficient.

Now we place a medium of length L composed of N atoms into a unidirectional ring cavity as shown in Fig. 2. In this figure, the reflection and transmission coefficients of mirrors M1 and M2 are R and T with $R + T = 1$. We assume that both mirrors M3 and M4 are perfect reflectors. In the ring cavity configuration, only the probe field E_p is circulated in the ring cavity but the driving fields E_c and E_s do not.

The total electromagnetic field can be written as

$$E = E_p e^{-i\omega_p t} + E_c e^{-i\omega_c t} + E_s e^{-i\omega_s t} + c.c., \tag{39}$$

Under the slowly varying envelop approximation, the dynamic response of the probe field governed by Maxwell equations as follows:

$$\frac{\partial E_p}{\partial t} + c\frac{\partial E_p}{\partial z} = i\frac{\omega_p}{2\varepsilon_0}P(\omega_p) \tag{40}$$

where $P(\omega_p)$ is induced polarization by the probe field in the transition $|1\rangle \leftrightarrow |4\rangle$ and is given by:

$$P(\omega_p) = Nd_{41}\rho_{41} \tag{41}$$

Substituting Eq. (41) into Eq. (40), we obtain the field amplitude relation in the steady state as:

$$\frac{\partial E_p}{\partial z} = i\frac{N\omega_p d_{41}}{2c\varepsilon_0}\rho_{41} \tag{42}$$

For a single circulation of the probe field in the cavity, we denote probe the field at the start and the end of the sample is $E_p(0)$ and $E_p(L)$, respectively (see Fig. 2). For a perfectly tuned cavity, the boundary conditions in the steady state for the incident (E_p^I) and transmitted (E_p^T) probe fields are given by:

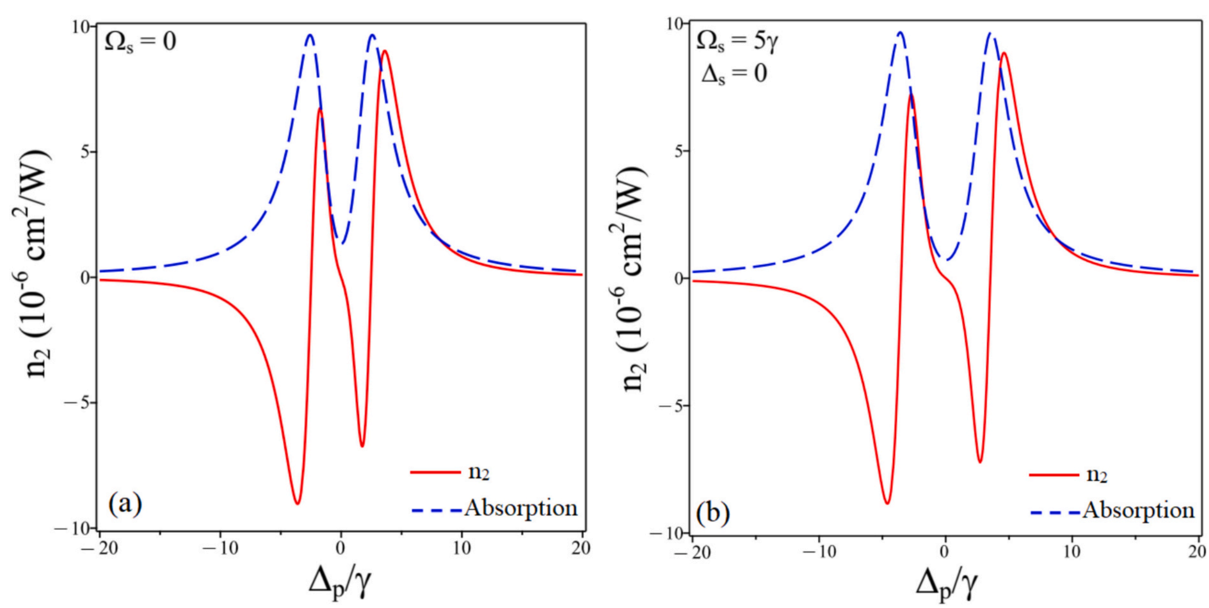

Fig. 3. Doppler-free. Kerr nonlinear coefficient (solid line) and absorption (dashed line) versus probe frequency detuning at different values of signal laser intensity $\Omega_s = 0$ (a) and $\Omega_s = 5\gamma$ (b). Other parameters as: $\Omega_c = 5\gamma$, $\Delta_c = 0$ and $\Delta_s = 0$.

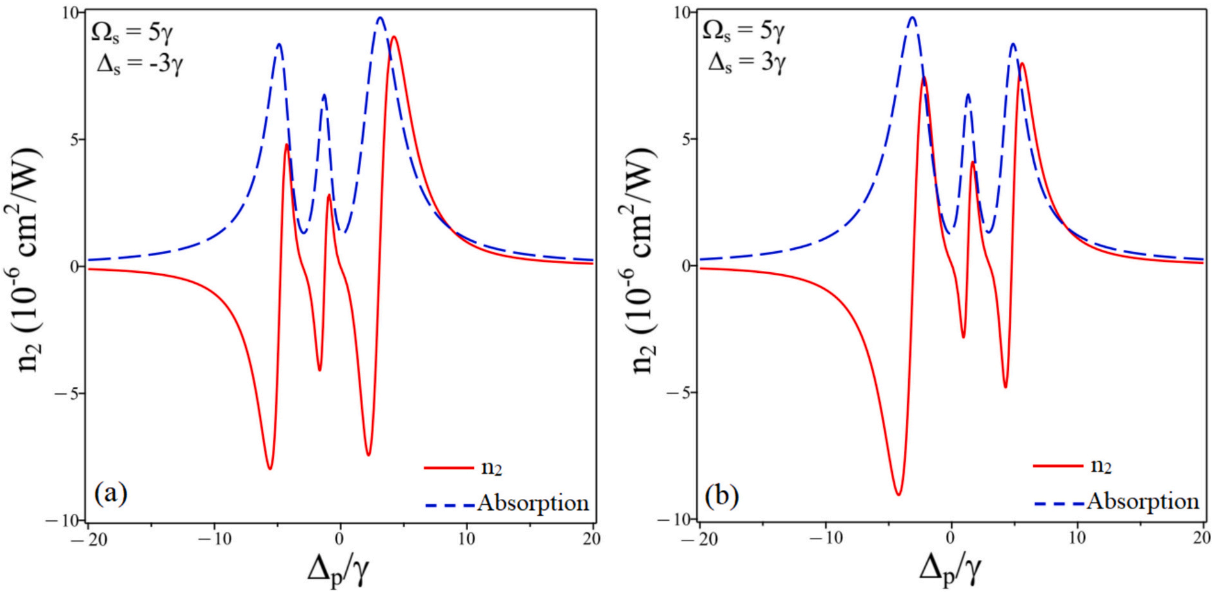

Fig. 4. Doppler-free. Kerr nonlinear coefficient (solid line) and absorption (dashed line) versus probe frequency detuning at different values of signal laser detuning $\Delta_s = -3\gamma$ (a) and $\Delta_s = 3\gamma$ (b) when $\Delta_c = 0$. Other parameters as: $\Omega_c = 5\gamma$ and $\Omega_s = 5\gamma$.

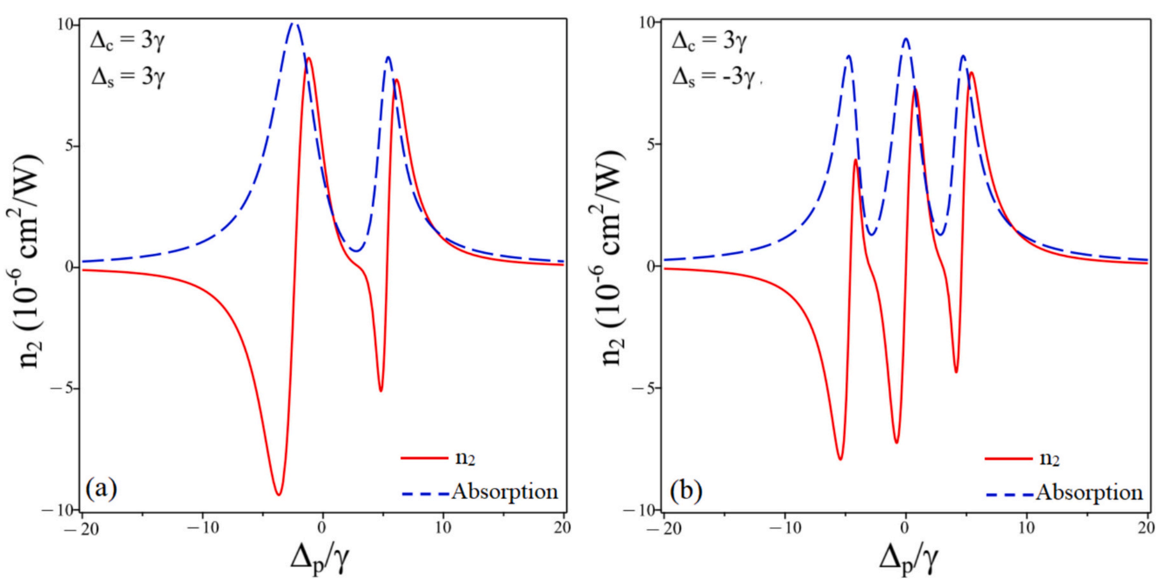

Fig. 5. Doppler-free. Kerr nonlinear coefficient (solid line) and absorption (dashed line) versus probe frequency detuning at different values of signal laser detuning $\Delta_s = -3\gamma$ (a) and $\Delta_s = 3\gamma$ (b) when $\Delta_c = 3\gamma$. Other parameters as: $\Omega_c = 5\gamma$ and $\Omega_s = 5\gamma$.

$$E_p(L) = E_p^T \Big/ \sqrt{T} \tag{43}$$

$$E_p(0) = \sqrt{T}E_p^I + RE_p(L) \tag{44}$$

where R is the feedback mechanism from the mirror M2, which is essential for the generation of bistability. We note that no bistability occurs if $R = 0$. In the mean-field limit and using of the boundary conditions, we obtain the following input-output relation for the transmitted probe field as:

$$Y = X - iC\rho_{41} \tag{45}$$

where $Y = d_{41}E_p^I/(\hbar\sqrt{T})$, $X = d_{41}E_p^T/(\hbar\sqrt{T})$ are normalized input and output probe fields, respectively, and $C = \frac{N\omega_p L d_{41}^2}{2c\varepsilon_0\hbar T}$ is the cooperatively parameter for atoms in the ring cavity. Thus, transmitted field depends on the incident probe field and the coherence term ρ_{41} via Eq. (45). As a result, the bistability behavior of medium can be determined by atomic variables through ρ_{41} which can be numerically solved from the density matrix eqs. (3)–(13).

3. Results and discussion

In this section, ^{87}Rb atom [68] is used to simulate in the variant states, as follows:$|1\rangle = 5S_{1/2}, F = 1, m_F = 1$; $|2\rangle = 5S_{1/2}, F = 1, m_F = 0$; $|3\rangle = 5S_{1/2}, F = 1, m_F = -1$ and $|4\rangle = 5P_{3/2}, F = 2, m_F = 0$. Here, F denotes the quantum number of total angular moment at the investigating state. Quantities in frequency units are normalized to the decay rate γ of the transition $|4\rangle \rightarrow |1\rangle$.

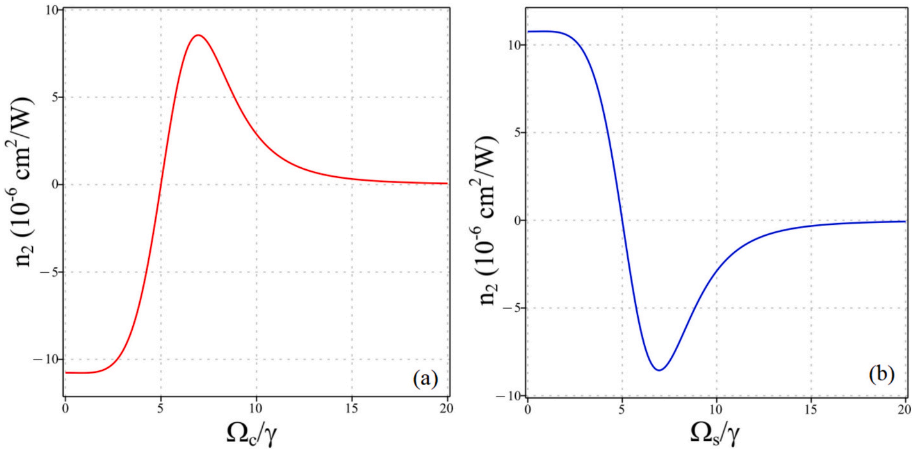

Fig. 6. Doppler-free. Kerr nonlinear coefficient versus coupling laser intensity when $\Omega_s = 5\gamma$ (a) and versus signal laser intensity when $\Omega_c = 5\gamma$ (b). Other parameters as $\Delta_p = 0$, $\Delta_c = 3\gamma$ and $\Delta_s = -3\gamma$.

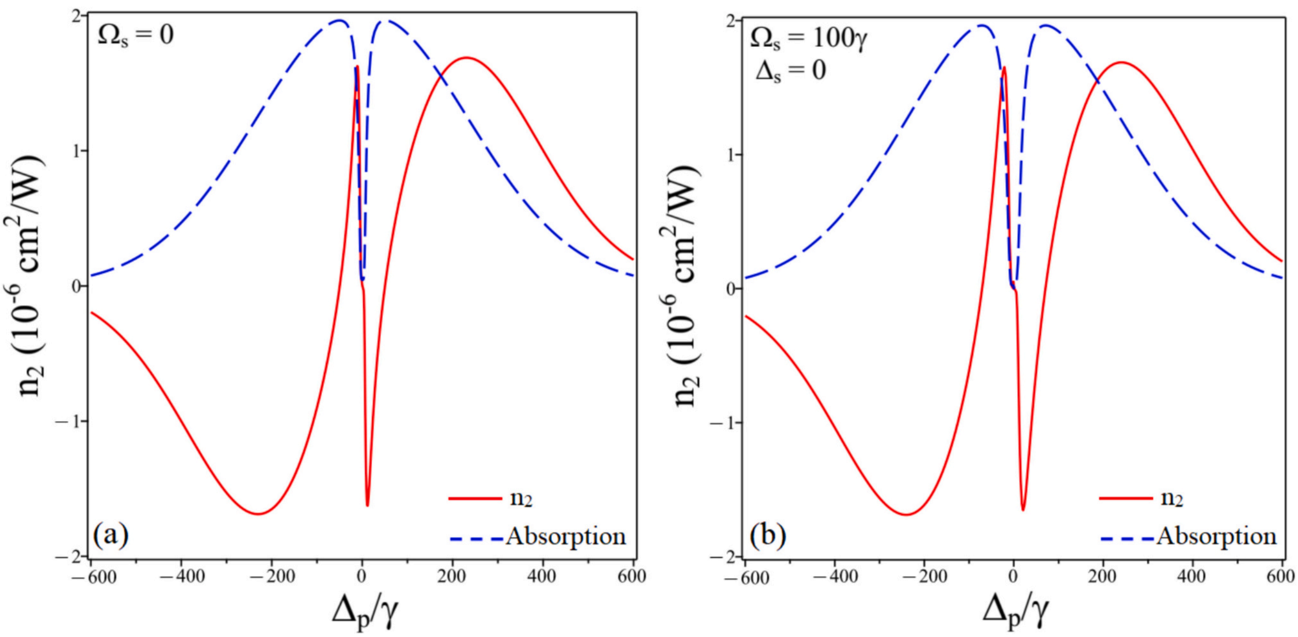

Fig. 7. Doppler broadening. Kerr nonlinear coefficient (solid line) and absorption (dashed line) versus probe frequency detuning at different values of signal laser intensity $\Omega_s = 0$ (a) and $\Omega_s = 100\gamma$ (b). Other parameters as: $\Omega_c = 100\gamma$, $\Delta_c = 0$, $\Delta_s = 0$ and T = 300 K.

3.1. Controlling Kerr nonlinear coefficient

In the absence of Doppler broadening: First, we investigate the influence of the signal laser intensity on the Kerr nonlinearity. Here, the controlling laser parameters is fixed at $\Omega_c = 5\gamma$ and $\Delta_c = 0$. Afterwards, we plot the absorption (dashed line) and Kerr nonlinear coefficient (solid line) versus the frequency detuning of the probe field at different values of signal laser intensity: (a) $\Omega_s = 0$ and (b) $\Omega_s = 5\gamma$ with $\Delta_s = 0$, as depicted in Fig. 3. In the case $\Omega_s = 0$, an EIT window appears at the center $\Delta_p = 0$ induced by the laser coupling field, and a pair of positive-negative peaks of the Kerr nonlinear coefficient appears around the center of the EIT window (Fig. 3a). When the signal laser beam is turned on with intensity $\Omega_s = 5\gamma$ and frequency $\Delta_s = \Delta_s = 0$, two EIT windows induced by the two driving fields appear and overlap each other at the center $\Delta_p = 0$ to form a slightly deeper and wider EIT window. This may result in a higher but less steep nonlinear dispersion curve (Fig. 3b). To separate into two distinct EIT windows we can adjust the signal laser frequency as shown in Fig. 4, here $\Delta_s = -3\gamma$ (a) and $\Delta_s = 3\gamma$ (b) while $\Omega_s = \Omega_c = 5\gamma$. It is clear that when $\Delta_s = -3\gamma$ the EIT window induced by the signal laser is shifted to the left to the position $\Delta_p = -3\gamma$, while $\Delta_s = 3\gamma$ it is shifted to the right to the position $\Delta_p = 3\gamma$. Correspondingly, two nonlinear dispersion curves are also generated at the two EIT windows and thus two pairs of Kerr nonlinear peaks are formed around these two EIT windows. The same phenomenon occurs if we fix the signal laser frequency and change the coupling laser frequency as shown in Fig. 5, where $\Delta_c = 3\gamma$ (a) and $\Delta_c = -3\gamma$ (b), with $\Delta_s = 3\gamma$ for both (a) and (b). It is shown that when $\Delta_c = \Delta_s = 3\gamma$ both EIT windows coincide at the position $\Delta_p = 3\gamma$ and therefore only one pair of Kerr nonlinear peaks appears around this position. When $\Delta_c = -3\gamma$ the EIT window induced by the coupling beam is shifted to the left to the position $\Delta_p = -3\gamma$ so there are two separate EIT windows symmetrically about $\Delta_p = 0$, i.e., in this case the absorption is maximum at the probe resonance frequency. Two pairs of Kerr nonlinear peaks are also formed around these two positions. Thus, by changing either the signal laser frequency or the coupling laser frequency, a single window EIT or a double window EIT is established and thus one or two pairs of Kerr nonlinear peaks are

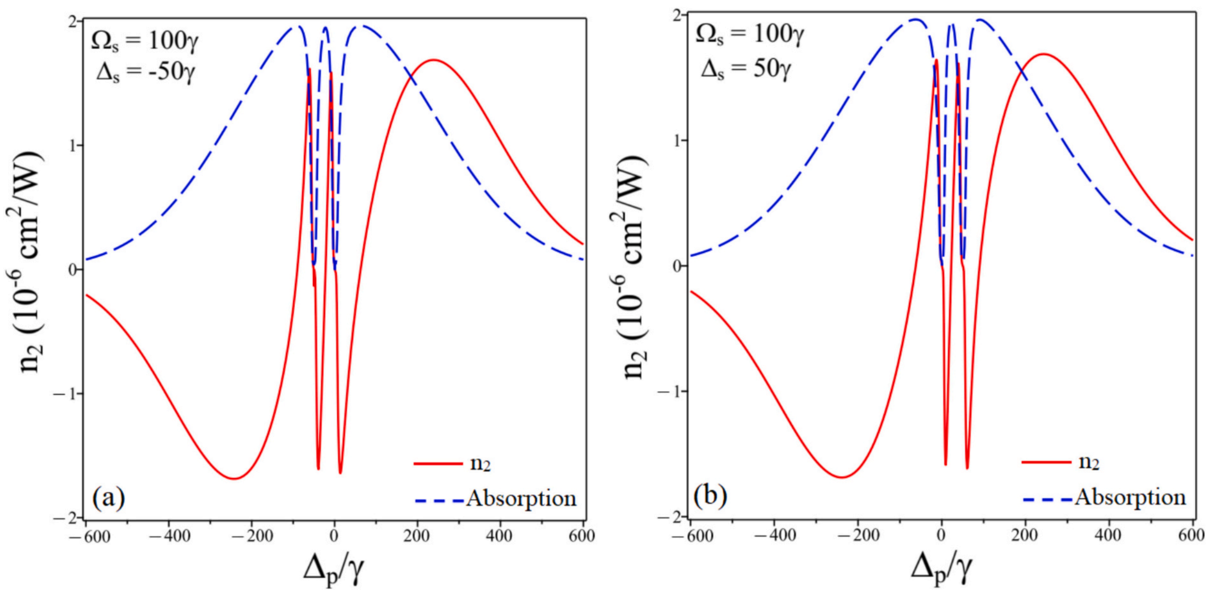

Fig. 8. Doppler broadening. Kerr nonlinear coefficient (solid line) and absorption (dashed line) versus probe frequency detuning at different values of signal laser detuning $\Delta_s = -50\gamma$ (a) and $\Delta_s = 50\gamma$ (b) when $\Delta_c = 0$. Other parameters as: $\Omega_c = 100\gamma$, $\Omega_s = 100\gamma$ and T = 300 K.

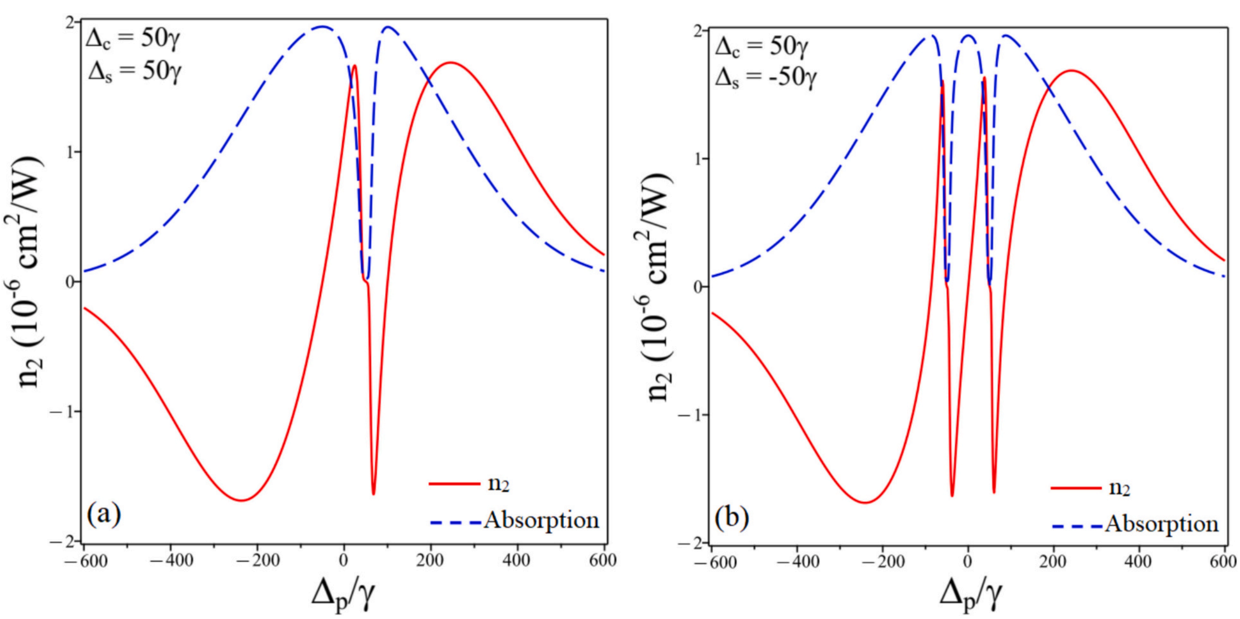

Fig. 9. Doppler broadening. Kerr nonlinear coefficient (solid line) and absorption (dashed line) versus probe frequency detuning at different values of signal laser detuning $\Delta_s = -50\gamma$ (a) and $\Delta_s = 50\gamma$ (b) when $\Delta_c = 50\gamma$. Other parameters as: $\Omega_c = \Omega_s = 100\gamma$ and T = 300 K.

generated around these EIT windows. At the same time, the position of the EIT windows and the Kerr nonlinear peaks are also shifted to different probe frequencies. This provides the opportunity to operate photonic devices at different laser frequencies simultaneously.

In Fig. 6, we fix the frequency of the laser fields at $\Delta_p = 0$, $\Delta_c = 3\gamma$ and $\Delta_s = -3\gamma$, and examine the variation of the Kerr nonlinear coefficient with respective to the intensity of the coupling laser (a) when $\Omega_s = 5\gamma$ and with respective to the signal laser (b) when $\Omega_c = 5\gamma$. Thus, at a given probe frequency $\Delta_p = 0$, the Kerr nonlinear coefficient changes both its amplitude and sign when adjusting the intensity of either the coupling laser or the signal laser. However, the variation of the Kerr nonlinear coefficient with the signal laser intensity is opposite to that with the laser coupling intensity. Such a change of the Kerr nonlinear coefficient will also lead to a change in the characteristics of the nonlinear optical effects, which will be considered in the following section.

In the presence of Doppler broadening: The investigations are performed in a similar way to the case without Doppler broadening. However, unlike the case without Doppler broadening, at room temperature under the Doppler effect, the EIT effect occurs with the driving laser field intensity tens of times larger than in the Doppler-free case. Likewise, the absorption and dispersion profiles are also broadened to hundreds of MHz. Specifically, in Fig. 7 we consider at temperature $T =$ 300 K and choose coupling laser intensity at $\Omega_c = 100\gamma$ and $\Delta_c = 0$, the graphs of absorption and Kerr nonlinear coefficients are plotted at $\Omega_s =$ 0 (a) and $\Omega_s = 100\gamma$ with $\Delta_c = 0$ (b). In this case, the phenomenon occurs similar to that in Fig. 3, but the difference is that the absorption spectrum is extended to more than 800 MHz. The EIT windows are also

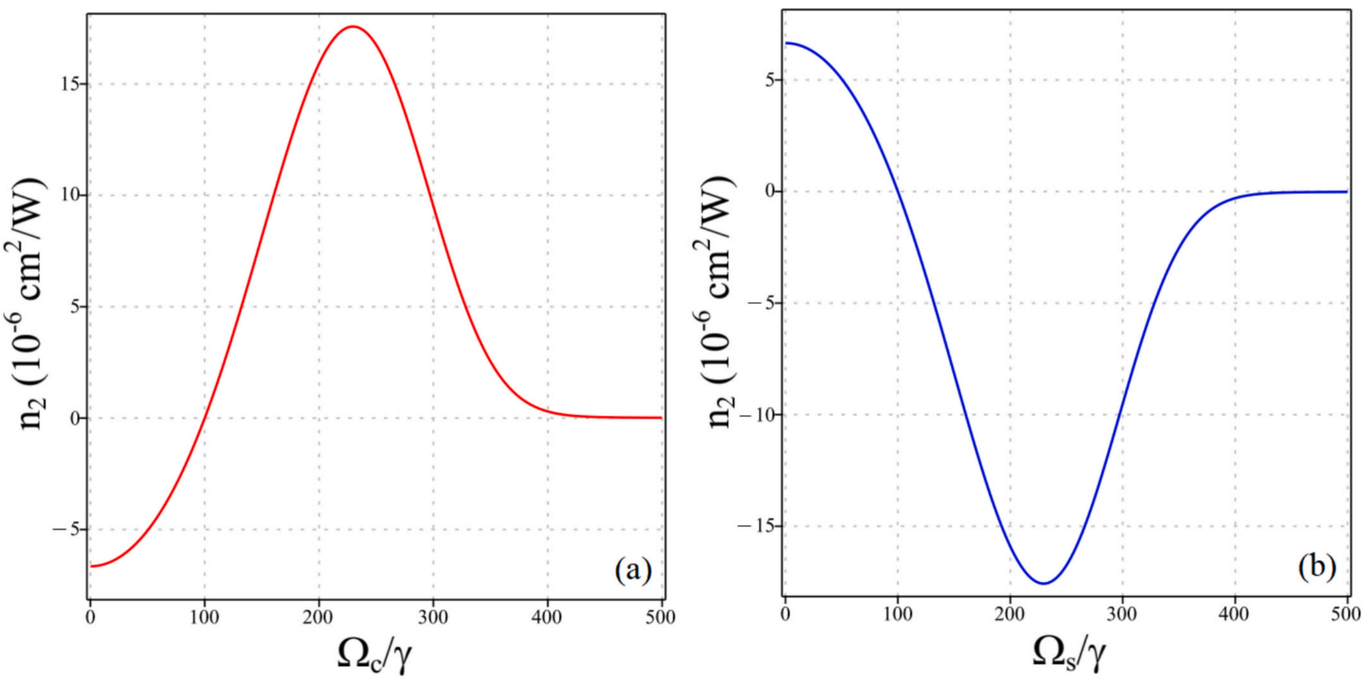

Fig. 10. Doppler broadening. Kerr nonlinear coefficient versus coupling laser intensity when $\Omega_s = 100\gamma$ (a) and versus signal laser intensity when $\Omega_c = 100\gamma$ (b). Other parameters as $\Delta_p = 0$, $\Delta_c = 50\gamma$, $\Delta_s = -50\gamma$ and T = 300 K.

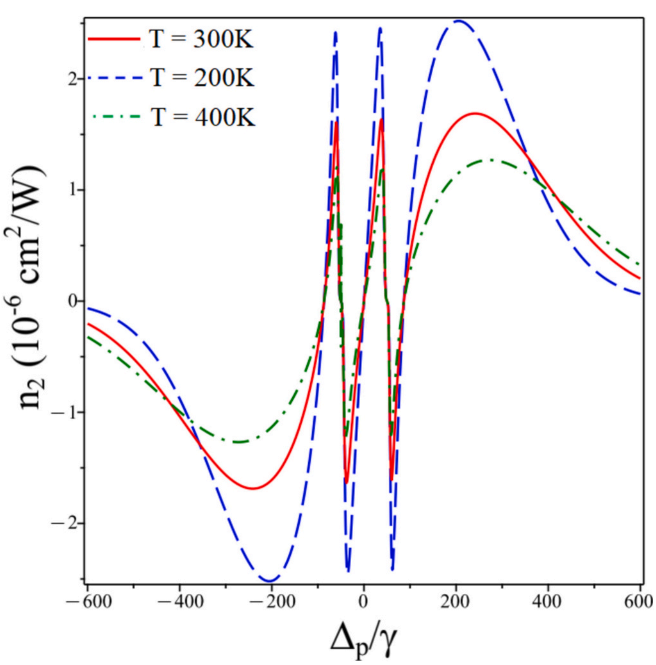

Fig. 11. Doppler broadening. Kerr nonlinear coefficient versus temperature when $\Omega_c = \Omega_s = 100\gamma$, $\Delta_c = 50\gamma$ and $\Delta_s = -50\gamma$.

separated when changing the coupling laser frequency or the signal laser frequency as shown in Figs. 8 and 9. Specifically, in Fig. 8(a) with $\Delta_c = 0$ and $\Delta_s = -50\gamma$, the positions of the two EIT windows are respectively $\Delta_p = 0$ (induced by the coupling beam) and $\Delta_p = -50\gamma$ (induced by the signal beam); in Fig. 8(b) with $\Delta_s = 50\gamma$, the EIT window induced by the signal beam is moved to position $\Delta_p = 50\gamma$. When $\Delta_c = \Delta_s = 50\gamma$, the two EIT windows overlap at $\Delta_p = 50\gamma$, and when $\Delta_c = 50\gamma$ and $\Delta_s = -50\gamma$, the two EIT windows are located at positions $\Delta_p = -50\gamma$ and $\Delta_p = 50\gamma$. In such cases, the Kerr nonlinear peak pairs also emerge around the corresponding EIT windows. The variations of the Kerr nonlinear coefficient with the coupling laser intensity (a) and the signal laser intensity (b) at room temperature T = 300 K are also shown in Fig. 10. Similar to Fig. 6, by changing the coupling or signal laser intensity, the magnitude and the sign of the Kerr nonlinear coefficient are also changed. However, unlike Fig. 6, in the case of Doppler broadening, the variation range of the coupling or signal laser intensity is relatively large. To examine the influence of temperature on the Kerr nonlinear coefficient, we simulate the Kerr nonlinear coefficient at different temperatures as shown in Fig. 11. Here, we fix the laser parameters at $\Omega_c = \Omega_s = 100\gamma$, $\Delta_c = 50\gamma$ and $\Delta_s = -50\gamma$, and plot the Kerr nonlinear coefficient with respective to the probe laser frequency at temperatures $T = 200$ K, 300 K and 400 K. It is obvious that the amplitude of the nonlinear dispersion curve increases significantly as the temperature of the atomic medium decreases. This phenomenon is directly related to the EIT efficiency that as the temperature decreases, the quantum interference is better, so the EIT efficiency is also better.

To demonstrate the superiority of this Kerr nonlinear medium, it is introduced into a ring resonator as shown in Fig. 2 to create an optical bistability effect. Here, we consider the Doppler-free case. In Fig. 12(a), we simulate the OB curve of the probe laser field at different probe frequencies around the atomic resonance frequency, while the driving laser parameters are fixed at $\Omega_c = \Omega_s = 5\gamma$ and $\Delta_c = \Delta_s = 0$. Fig. 12(b) depicts the variation of the Kerr nonlinearity coefficient (solid line) and absorption coefficient (dashed line) versus the probe laser frequency with the same driving laser parameters as in Fig. 12(a). From Fig. 12(a), it can be seen that the threshold intensity and width of OB at different probe laser frequencies are very different. This phenomenon is closely related to both the Kerr nonlinear coefficient and the absorption coefficient. In principle, the smaller the absorption coefficient, the lower the threshold intensity of OB and vice versa, the higher the absorption coefficient, the higher the threshold intensity. Meanwhile, the magnitude of the Kerr nonlinear coefficient determines the formation of the OB effect and the width of OB depends sensitively on the amplitude of the Kerr nonlinear coefficient. Specifically, at the probe laser frequency $\Delta_p = 0$, although the absorption is very small, close to zero (the dashed line in Fig. 12b), the Kerr nonlinear coefficient is also close to zero (the solid

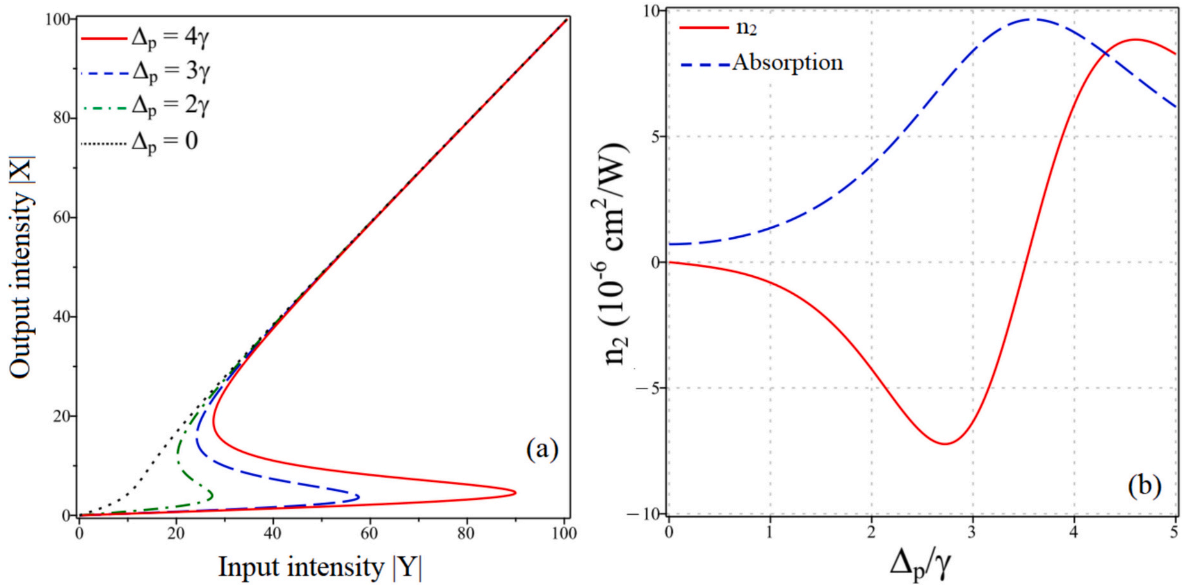

Fig. 12. OB graphs at different values of probe laser detuning when $\Omega_c = \Omega_s = 5\gamma$ and $\Delta_c = \Delta_s = 0$.

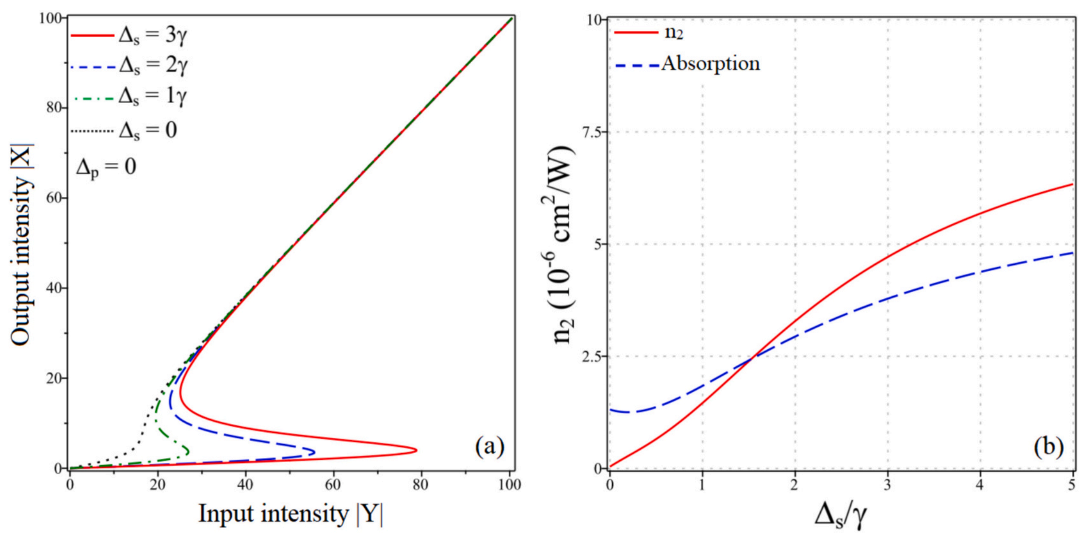

Fig. 13. OB graphs at different values of signal laser detuning when $\Delta_p = 0$, $\Delta_c = -3\gamma$ and $\Omega_c = \Omega_s = 5\gamma$.

line in Fig. 12b), so the OB effect does not appear yet (see the dotted line in Fig. 12a). At the probe laser frequencies $\Delta_p = 2\gamma$, 3γ, and 4γ, the amplitude of the Kerr nonlinear coefficient gradually increases, causing the OB effect to appear with the OB width also increasing. At the same time, the growth of the absorption coefficient results in the increase of the OB threshold intensity. As a result, in Fig. 12, at the probe resonance frequency $\Delta_p = 0$, the OB does not appear due to the zero Kerr nonlinearity, however, this situation can be changed by adjusting the frequency of the driving lasers. Indeed, in Figs. 13 and 14 we fix the probe laser frequency at $\Delta_p = 0$ and change the signal laser frequency (Fig. 13) and the coupling laser frequency (Fig. 14). According to Fig. 13, it is clear that when $\Delta_s = 0$, the OB does not appear due to the zero Kerr nonlinearity (the solid line in Fig. 13a). By gradually increasing the signal laser frequency detuning, the Kerr nonlinear amplitude is also increased (the solid line in Fig. 13b), so the OB appears with its width also increasing. In addition, the threshold intensity of the OB also increases due to the enhanced absorption when Δ_s increases. The same phenomenon occurs when increasing the coupling laser frequency detuning as shown in Fig. 14. Specifically, the increase in Δ_c leads to the increase of the threshold intensity and the width of OB. On the other hand, from our previous analyses, the advantage of this four-level lambda model is the appearance of many Kerr nonlinear pairs around the EIT windows. As a result, the OB effect can also be obtained at different probe frequency domains. Indeed, Fig. 15 shows the appearance of the OB effect at the resonant (a) and far-resonant (b) domains. In a similar way, we can obtain the OB effect at other frequency domains by changing the frequency of the driving laser fields. Finally, in Fig. 16(a) we examine the variation of the threshold intensity and the width of OB with the signal laser intensity. Here, the probe laser frequency is chosen at $\Delta_p = 2\gamma$ and other laser parameters are $\Delta_s = \Delta_c = 0$ and $\Omega_c = 5\gamma$. Fig. 16(b) shows that both the Kerr nonlinearity and the absorption coefficients decrease with increasing signal laser intensity, so the threshold intensity and the width of OB decrease with increasing signal laser intensity. Because the roles of the coupling and signal fields are the same, a similar examination with the coupling laser intensity is not shown further.

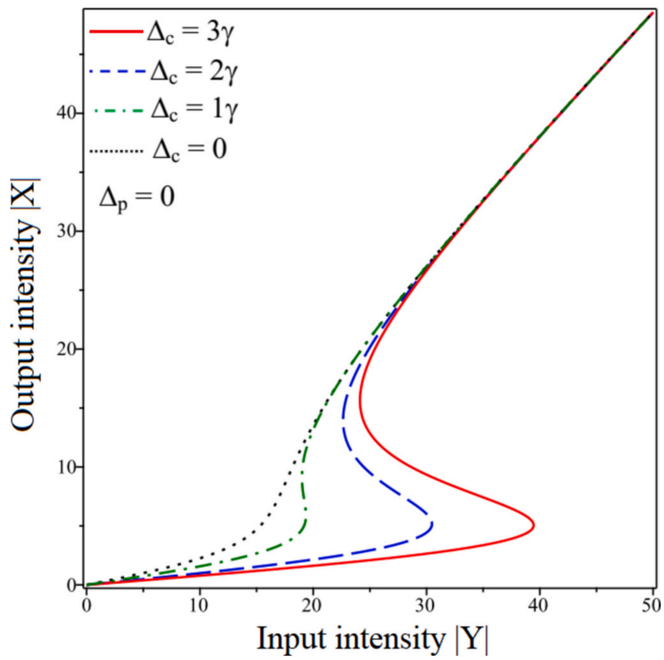

Fig. 14. OB graphs at different values of coupling laser detuning when $\Delta_p = 0$, $\Delta_s = 3\gamma$ and $\Omega_c = \Omega_s = 5\gamma$.

4. Conclusion

In conclusion, we have demonstrated the enhancement and the control of the Kerr nonlinear coefficient by driving laser fields in the ^{87}Rb atomic gas medium of four-level lambda-type configuration. By changing the coupling laser frequency or the signal laser frequency, a single-window or double-window EIT response is formed. In each such EIT window, a pair of positive-negative peaks of the Kerr nonlinear coefficient appears. Furthermore, the amplitude and the sign of the Kerr nonlinear coefficient changes with respect to the frequency or the intensity of the driving laser fields. In particular, the Doppler effect is also included in the expression of the Kerr nonlinear coefficient, which has a realistic value when the model is applied at room temperature. At room temperature, the EIT effect as well as the enhancement of the Kerr nonlinearity occurs with laser intensities tens of times larger than when Doppler is ignored; it is also shown that at room temperature, the EIT spectrum profile as well as the nonlinear dispersion curve are broadened to hundreds of MHz, while the amplitude of the nonlinear dispersion curve decreases with increasing temperature. To demonstrate the superiority of such Kerr nonlinearity, we have applied this model to an atomic optical bistability system. The emergence of Kerr nonlinear coefficient around the EIT windows is the key basis for the appearance of low-threshold OB effect. The changes in the amplitude and the sign of Kerr nonlinear coefficient lead to changes in the threshold intensity and the width of OB. In particular, in the double-window EIT regime, we can obtain the OB curves at different frequency domains simultaneously, which allows its applications to operate on multiple frequency channels. Such investigations are necessary for experimental observations and related studies.

Authorship contribution statement

All authors conceived of the presented idea, developed the theory and performed the analytical calculations and numerical simulations. All authors co-wrote the paper, discussed the results and contributed to the final manuscript.

CRediT authorship contribution statement

Luong Thi Yen Nga: Writing – review & editing, Writing – original draft, Software, Methodology, Investigation, Formal analysis. **Nguyen Huy Bang:** Writing – review & editing, Writing – original draft, Software, Methodology, Investigation, Formal analysis. **Nguyen Van Phu:** Writing – review & editing, Writing – original draft, Software, Methodology, Investigation, Formal analysis. **Hoang Minh Dong:** Writing – review & editing, Writing – original draft, Software, Methodology, Investigation, Formal analysis. **Nguyen Thi Thu Hien:** Writing – review & editing, Writing – original draft, Software, Methodology, Investigation, Formal analysis. **Nguyen Van Ai:** Writing – review & editing, Writing – original draft, Software, Methodology, Investigation, Formal analysis. **Le Van Doai:** Writing – original draft, Software, Methodology, Investigation, Formal analysis.

Declaration of competing interest

The authors declare that they have no known competing financial

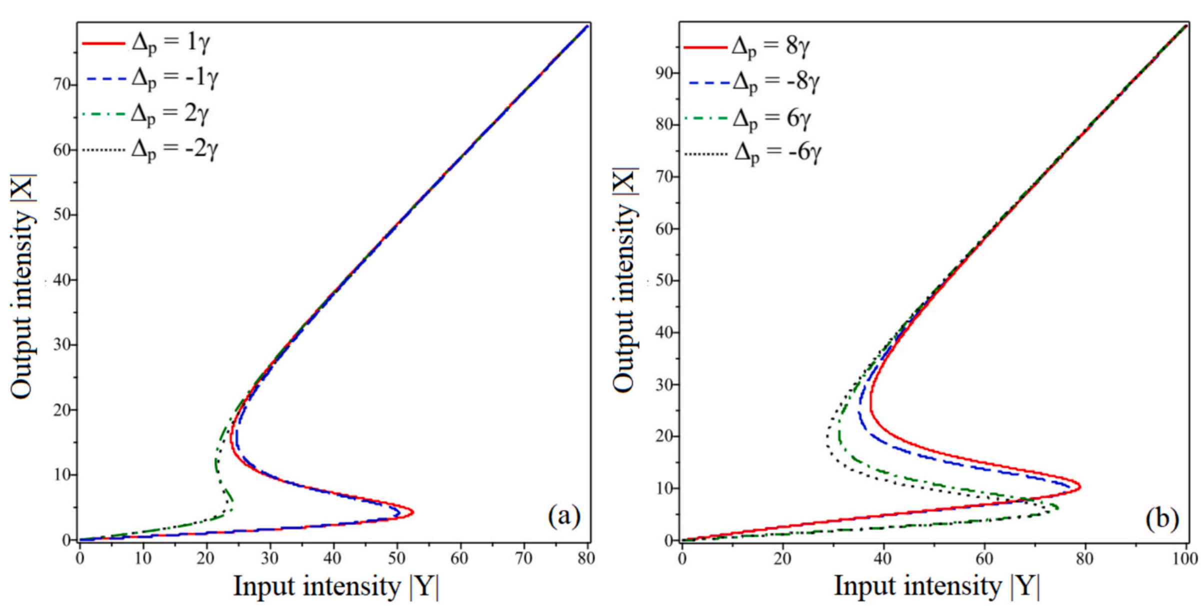

Fig. 15. OB graphs at different values of probe laser detuning when $\Delta_c = -3\gamma$, $\Delta_s = 3\gamma$ and $\Omega_c = \Omega_s = 5\gamma$.

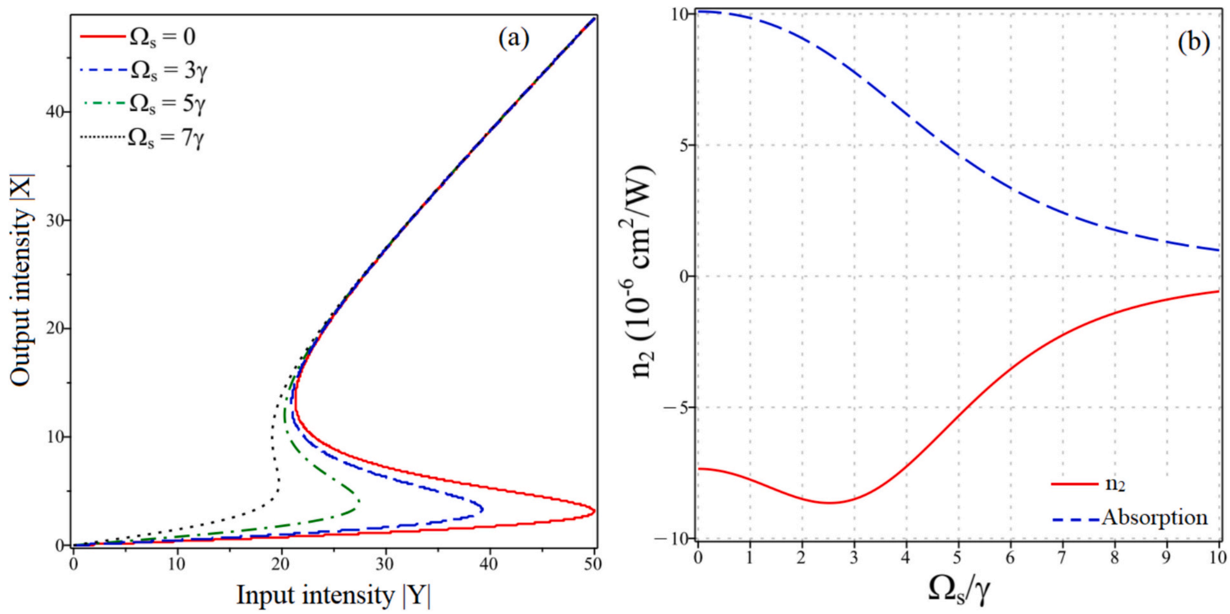

Fig. 16. OB graphs at different values of signal laser intensity when $\Delta_p = 2\gamma$, $\Delta_s = \Delta_c = 0$ and $\Omega_c = 5\gamma$.

interests or personal relationships that could have appeared to influence the work reported in this paper.

Acknowledgment

This research was funded by Vingroup Innovation Foundation (VINIF) under project code VINIF.2022.DA00076.

Data availability

No data was used for the research described in the article.

References

[1] Boyd RW. Nonlinear optics 4th. Academic Press; 2020.
[2] Boller K-J, Imamoğlu A, Harris SE. Observation of electromagnetically induced transparency. Phys Rev Lett 1991;66(20):2593–6.
[3] Schmidt H, Imamogdlu A. Giant Kerr nonlinearities obtained by electromagnetically induced transparency. Opt Lett 1996;21:1936.
[4] Kang H, Zhu Y. Observation of large Kerr nonlinearity at low light intensities. Phys Rev Lett 2003;91:093601.
[5] Harris SE, Field JE, Imamoğlu A. Nonlinear optical processes using electromagnetically induced transparency. Phys Rev Lett 1990;64(10):1107–10.
[6] Harris SE, Hau LV. Nonlinear optics at low light levels. Phys Rev Lett 1999;82: 4611.
[7] Bang NH, Khoa DX, Doai LV. Controllable optical properties of multi-electromagnetically induced transparency gaseous atomic medium. Commun. Phys. 2019;28:1–33.
[8] Li YQ, Xiao M. Electromagnetically induced transparency in a three-level Λ-type system in rubidium atoms Phys. Rev A 1995;51:2703–6.
[9] Hopkins SA, Usadi E, Chen HX, Durrant AV. Electromagnetically induced transparency of laser-cooled rubidium atoms in three-level Λ-type systems. Opt Comm 1997;138:185–92.
[10] Li YQ, Xiao M. Electromagnetically induced transparency in ladder-type inhomogeneously broadened media: theory and experiment. Phys Rev A 1995;51: 576–84.
[11] Welch G, Padmabandu G, Fry E, Lukin M, Nikonov D, Sander F, et al. Observation of V-type electromagnetically induced transparency in a sodium atomic beam. Found Phys 1998;28:621–38.
[12] Chen Y, Wei XG, Ham BS. Optical properties of an N-type system in Doppler-broadened multilevel atomic media of the rubidium D_2 line. J Phys B: At Mol Opt Phys 2009;42:065506.
[13] Qi J. Electromagnetically induced transparency in an inverted Y-type four-level system. Phys Scr 2009;81(1):015402.
[14] Zhang L. The electromagnetically induced transparency in the Y-type four-level atom system at low light levels. Sci China Ser G 2005;48(5):593.
[15] Li S, Yang X, Cao X, Xie C, Wang H. Two electromagnetically induced transparency windows and an enhanced electromagnetically induced transparency signal in a four-level tripod atomic system. J. Phys. B: At. Mol. Opt. Phys. 2007;40:3211–9.
[16] McGloin D, Fullton DJ, Dunn MH. Electromagnetically induced transparency in *N*-level cascade schemes. Opt Commu 2001;190:221.
[17] Paspalakis E, Knight PL. Electromagnetically induced transparency and controlled group velocity in a multilevel system. Phys Rev A 2002;66:015802.
[18] Wang J, Kong LB, Tu XH. Electromagnetically induced transparency in multi-level cascade scheme of cold rubidium atoms. Phys Lett A 2004;328:437.
[19] Doai LV, Trong PV, Khoa DX, Bang NH. Electromagnetically induced transparency in five-level cascade scheme of ^{85}Rb atoms: an analytical approach. Optik 2014; 125:3666–9.
[20] Yu H, Kim KS, Kim JD, Lee HK, Kim JB. Observation of Doppler-free electromagnetically induced transparency in atoms selected optically with specific velocity. Phys Rev A 2011;84:052511.
[21] Cox K, Yudin VI, Taichenachev AV, Novikova I, Mikhailov EE. Measurements of the magnetic field vector using multiple electromagnetically induced transparency resonances in Rb vapor. Phys Rev A 2011;83:015801.
[22] Ying K, Niu Y, Chen D, Cai H, Qu R, Gong S. Observation of multi-electromagnetically induced transparency in V-type rubidium atoms. J. Mod. Opt. 2014;61:631–5.
[23] Kumar R, Gokhroo V, Chormaic SN. Multi-level cascaded electromagnetically induced transparency in cold atoms using an optical nanofibre interface. New J Phys 2015;17:123012.
[24] Khoa DX, Trung LC, Thuan PV. Measurement of dispersive profile of a multiwindow electromagnetically induced transparency spectrum in a Doppler-broadened atomic medium. J. Opt. Soc. Am. B 2017;34:1255.
[25] Bang NH, Ai NV, Son DH, Thuan PV, Nga LTY, Quang HH, et al. Observation of giant group index in a multi-level ^{85}Rb atomic medium at room temperature. J. Opt. Soc. Am. B 2017;34:1255.
[26] Sen S, Dey TK, Nath MR, et al. Comparison of electromagnetically induced transparency in lambda, cascade and vee three-level systems. J. Mod. Opt. 2015;62 (3):166–74.
[27] Wang H, Goorskey D, Xiao M. Enhanced Kerr nonlinearity via atomic coherence in a three-level atomic system. Phys Rev Lett 2001;87:073601-1–1–4.
[28] Y. Han, J. Xiao, Y. Liu, C. Zhang, H. Wang, M. Xiao, and K. Peng, "Interacting dark states with enhanced nonlinearity in an ideal four-level tripod atomic system," Phys. Rev. A77, (2008)023824.
[29] Yang X, Li S, Zhang C, Wang H. Enhanced cross-Kerr nonlinearity via electromagnetically induced transparency in a four-level tripod atomic system. J. Opt. Soc. Am. B. 2009;26:1423.
[30] Sahrai M, Asadpour SH, Sadighi R. Enhanced Kerr nonlinearity in a four-level EIT medium. J Nonlinear Optic Phys Mat 2010;19:503.
[31] Liang H, Niu, Y.p., Deng, L. & Gong, S.q.. Enhancement of Kerr nonlinearity completely without absorption. Phys. Lett. A 2017;381:3978–82.
[32] Sahrai M, Hamedi HR, Memarzadeh M. Kerr nonlinearity and optical multi-stability in a four-level Y-type atomic system. J. Mod. Opt. 2012;59(11):980–7.
[33] Hamedi HR, Juzeliunas G. Phase-sensitive Kerr nonlinearity for closed-loop quantum systems. Phys Rev A 2015;91:053823.
[34] D. X. Khoa, L. V. Doai, D. H. Son, and N. H. Bang, "Enhancement of self-Kerr nonlinearity via electromagnetically induced transparency in a five-level cascade system: an analytical approach," J Opt Soc Am B, 31, N**6** (2014) 1330.
[35] N. H. Bang & L. V. Doai, "Colossal Kerr nonlinearity without absorption in a five-level atomic medium.", Sci Rep 14, (2024) 1554 (11pp).
[36] Tian S-C, Wan R-G, Tong C-Z, Ning Y-Q, Qin L, Liu Y. Giant Kerr nonlinearity induced by tunneling in triple quantum dot molecules. J. Opt. Soc. Am. B 2014;31: 1436–42.

[37] Terzis AF, Kosionis SG, Boviatsis J, et al. Nonlinear optical susceptibilities of semiconductor quantum dot-metal nanoparticle hybrids. J Mod Opt 2015;63(5): 451–61.
[38] Akram H, Al-Khursan Amin H. Second-order nonlinearity in ladder-plus-Y configuration in double quantum dot structure. Appl Optics 2016;55:9866–74.
[39] Nath M, Mukherjee R, Borgohain N. Giant Kerr-quintic-septic nonlinearities in semiconductor quantum wells. Eur Phys J Plus 2022;137:903.
[40] Nath M, Mukherjee R, Borgohain N, Hazra R. Phase-sensitive large Kerr nonlinearity in semiconductor quantum wells. Mod Phys Lett B 2024;38(25): 2450238.
[41] Naseri T, Maleki Z. Theoretical study of enhanced Kerr nonlinearity in nanohybrid structures resulting from interactions between plasmonic modes and excitonic transitions. Opt Continuum 2024;3:1555–67.
[42] Guo Y-W, Xu S-L, He J-R, Deng P, Belić MR, Zhao Y. Transient optical response of cold Rydberg atoms with electromagnetically induced transparency. Phys Rev A 2020;101:023806.
[43] Liao Q-Y, Hu H-J, Chen M-W, Shi Y, Zhao Y, Hua C-B, et al. Two-dimensional spatial optical solitons in Rydberg cold atomic system under the action of optical lattice. Acta Phys Sin 2023;72:104202.
[44] Sheng J, Yang X, Wu H, Xiao M. Modified self-Kerr-nonlinearity in a four-level N-type atomic system. Phys Rev A 2011;84:053820.
[45] X. Yang, K. Ying, Y. Niu and S. Gong, "Reversible self-Kerr-nonlinearity in an N-type atomic system through a switching field", J Opt 17 (2015) 045505 (5pp).
[46] Anton MA, Calderon Oscar G. Optical bistability using quantum interference in V -type atoms. J Opt B: Quantum Semiclass Opt 2002;4:91–8.
[47] Joshi A, Brown A, Wang H, Xiao M. Controlling optical bistability in a three-level atomic system. Phys Rev A 2003;67:041801(R).
[48] Li J. Coherent control of optical bistability in a microwave-driven V-type atomic system. Physic D 2007;228:148.
[49] Wang Zhen, Chen Ai-Xi, Bai Yanfeng, Yang Wen-Xing, Lee Ray-Kuang. Coherent control of optical bistability in an open Λ-type three-level atomic system. J Opt Soc Am B 2012;29(10):2891–6.
[50] Doai LV, Phuong LTM, Anh NT, Son DH, Sau VN, Khoa DX, et al. A comparative study of optical bistability in three-level EIT configurations. Commun Phys 2018; 28:127–38.
[51] Li JH, Lu XY, Luo JM, Huang QJ. Optical bistability and multistability via atomic coherence in an N-type atomic medium. Phys Rev A 2006;74:035801.
[52] Lu XY, Li JH, Liu JB, Luo JM. Optical bistability via quantum interference in a four-level atomic medium. J Phys B 2006;39:5161.
[53] Sahrai M, Asadpour SH, Mahrami H, Sadighi-Bonabi R. Controlling the optical bistability via quantum interference in a four-level N-type atomic system. J Lumines 2011;131:1682–6.
[54] Sahrai M, Hamedi HR, Memarzadeh M. Kerr nonlinearity and optical multi-stability in a four-level Y-type atomic system. J. Mod. Opt. 2012;59(11):980–7.
[55] Hamedi HR, Asadpour SH, Sahrai M, Arzhang B, Taherkhani D. Optical bistability and multi-stability in a four-level atomic scheme. Opt Quant Electron 2013;45(3): 295–306.
[56] Hien NTT, Dan NL, Bang NH, Khoa DX, Phu NV, Anh NTL, et al. Two-channel optical bistability and multistability in a degenerate four-level atomic medium under a static magnetic field. Sci Rep 2024;14:19007 [11pp].
[57] Ebrahimi Zohravi L, Doostkam R, Mousavi SM, Mahmoudi M. Controlling the optical bistability in a Kobrak-Rice 5-level quantum system. Progr Electrom Re M 2012;25:1–11.
[58] Khoa DX, Doai LV, Anh LNM, Trung LC, Thuan PV, Dung NT, et al. Optical bistability in a five-level cascade EIT medium: an analytical approach. J. Opt. Soc. Am. B 2016;33(4):735–40.
[59] Dong HM, Hien NTT, Bang NH, Doai LV. Dynamics of twin pulse propagation and dual-optical switching in a $\Lambda + \Xi$ atomic medium. Chaos, Solitons and Fractals 2024;178:114304.
[60] Bang NH, Anh LNM, Dung NT, Doai LV. Comparative study of light manipulation in three-level systems via spontaneously generated coherence and relative phase of laser fields. Commun Theo Phys 2019;71:947–54.
[61] Doai LV. Role of incoherent pumping field on control of optical bistability in a closed three-level ladder atomic system. Eur Phy J D 2020;74:171.
[62] Tian S-C, Wan R-G, Tong C-Z, Ning Y-Q. Controlling optical bistability via interacting double dark resonances in linear quantum dot molecules. J. Opt. Soc. Am. B 2014;31:2681–8.
[63] Hamedi HR. Optical bistability and multistability via magnetic field intensities in a solid. Appl Optics 2014;53:5391–7.
[64] Soltani A, Nasehi R, Asadpour SH, Mahmoudi M, Rahimpour Soleimani H. Investigation of optical bistability in a double InxGa1−xN/GaN quantum-dot nanostructure via inter-dot tunneling effect. Appl Optics 2015;54:2606–14.
[65] Asadpour SH, Solookinejad G, Panahi M, Sangachin EA. All-optical switching between optical bistability and multistability in a defect dielectric medium doped with a multiple quantum well nanostructure. Appl Optics 2016;55:722–7.
[66] Carre no F, Antón MA, Paspalakis E. Nonlinear optical rectification and optical bistability in a coupled asymmetric quantum dot-metal nanoparticle hybrid. J Appl Phys 2018;124(11):113107.
[67] Zhang H, Wang G, Sun D, Li XW, Sun H. Optical bistability and multistability induced by quantum coherence in diamond germanium-vacancy color centers. Appl Optics 2019;58:2522–9.
[68] Steck DA. ^{87}Rb D line data. http://steck.us/alkalidata; 2019.